

GeoFill: Reference-Based Image Inpainting of Scenes with Complex Geometry

Yunhan Zhao^{1*}, Connelly Barnes², Yuqian Zhou^{2,3}, Eli Shechtman², Sohrab Amirghodsi², Charless Fowlkes¹
¹UC Irvine ²Adobe Research ³IFP, UIUC

{yunhaz5, fowlkes}@ics.uci.edu {cobarnes, elishe, tamirgho}@adobe.com yuqian2@illinois.edu

Abstract

Reference-guided image inpainting restores image pixels by leveraging the content from another reference image. The previous state-of-the-art, TransFill, warps the source image with multiple homographies, and fuses them together for hole filling. Inspired by structure from motion pipelines and recent progress in monocular depth estimation, we propose a more principled approach that does not require heuristic planar assumptions. We leverage a monocular depth estimate and predict relative pose between cameras, then align the reference image to the target by a differentiable 3D reprojection and a joint optimization of relative pose and depth map scale and offset. Our approach achieves state-of-the-art performance on both RealEstate10K and MannequinChallenge dataset with large baselines, complex geometry and extreme camera motions. We experimentally verify our approach is also better at handling large holes.

1. Introduction

Image inpainting aims to plausibly restore missing pixels within a hole region that is selected by the user. Existing technologies mostly focus on single image inpainting in which convolutional neural network (CNN) models leverage knowledge learned from large scale training sets to fill in pixels [43, 49, 50]. Those methods achieve outstanding performance on some inputs but fail catastrophically on others. In cases where images are different from training data or hole regions are too large, single image inpainting models tend to be unreliable due to the ill-posed nature of the task itself.

Reference-guided image inpainting has been proposed to overcome the aforementioned difficulties by assuming that a second image is available that was taken from another viewpoint of the same scene. TransFill [62] is a state-of-the-art reference-guided inpainting method that fits multiple homographies to clusters of matching feature points and



Figure 1. Given a reference image and a target image with hole, GeoFill utilizes predicted correspondence matching and depth maps to estimate a 3D mesh and relative camera pose and intrinsics. Compared to TransFill, the previous state-of-the-art approach, GeoFill handles complex scenes better by iteratively refining predicted depth maps and relative pose.

warps the reference image using those homographies to produce candidate infill content. However, in a pinhole camera model, if the camera translates, a homography is only capable of modeling planar scene geometry. Real scenes rarely have only a few planar surfaces, and even when they do, it can be hard to identify the relevant planar surfaces. Thus, for scenes with complicated 3D structure near the hole that violates the homography assumption, clustering depths into planar surfaces becomes unreliable. Moreover, these problems worsen if the baseline between the cameras increases which can introduce more parallax or disocclusions that break the implicit planarity assumption.

To address the issues of homography-based methods, we propose a principled approach that fills the hole region by

*Work done while an intern at Adobe.

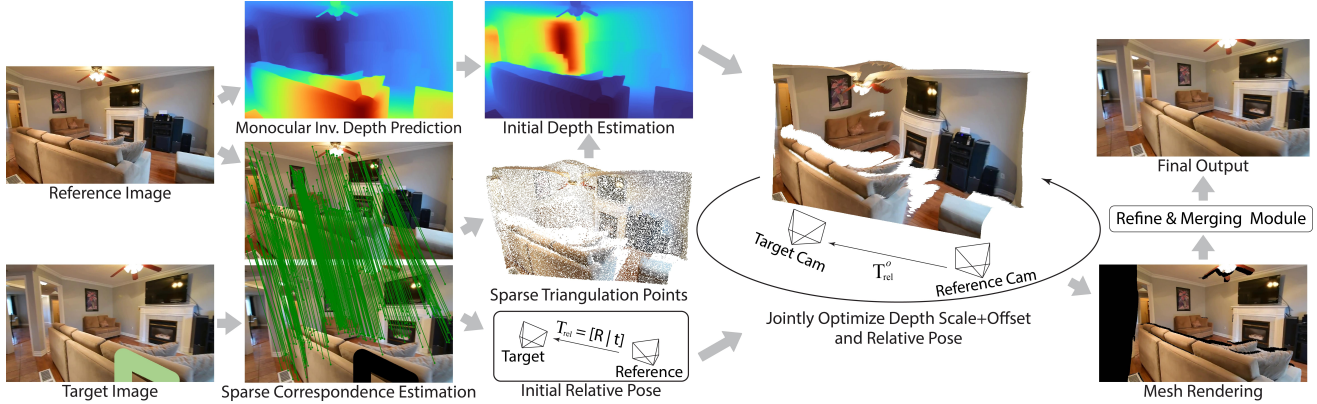


Figure 2. Overview of our system pipeline. We are given a reference image and a target image with hole indicated. Please see the introduction for a high-level discussion of the components.

first estimating the 3D scene structure from two views and then synthesizing candidate inpainting content by rendering a textured mesh. We show an overview of our pipeline in Figure 2. We first estimate sparse feature correspondences, from which we derive an initial relative pose between two views. We then predict a monocular dense depth map of the source image and determine a scale and offset that aligns the depth map with sparse 3D triangulated points. To mitigate the prediction errors and improve alignment accuracy, then we jointly optimize the depth scale and offset and the relative pose using a fast differentiable 3D reprojection of the reference image into the target image. We synthesize a warped source image by rendering a textured source mesh with the optimized depth and target pose, and fill disoccluded regions with a single image inpainting model. Lastly, we adjust the exposure, white balance, lighting, and correct any residual misalignments before pasting the result into the hole region to be filled. Our approach is inspired by Structure from Motion (SfM) pipelines, but unlike SfM-based approaches that can require ground-truth camera intrinsic parameters or more than two images, our approach works on arbitrary pairs of images that share overlapping scene content.

In summary, our contributions are: 1) To our knowledge, our approach is the first to leverage explicit non-planar 3D surfaces for reference-based image inpainting and achieves state-of-the-art performance. 2) Our approach better handles challenging cases such as complex 3D scene structures, wide-baseline image pairs, and large holes. 3) Our approach fills holes in a principled manner utilizing only a single proposal, which mitigates ghosting artifacts present in some TransFill results.

2. Related Work

Image inpainting. Traditional image inpainting models rely on hand-crafted heuristics. Diffusion-based ap-

proaches [5] propagate pixel colors from the background to the hole region. These approaches generate artifacts when the hole size is large or texture variations are significant. Alternatively, patch-based approaches [2, 42] search for similar patches outside the hole region to complete the missing regions. Although these approaches offers high quality texture by copying texture patches, the filled regions may be inconsistent with regions around the hole due to lack of high-level structural understanding of the entire image.

Recent deep models fill the hole by learning from large amounts of training data. Context encoders [33] generate semantically plausible content in the hole by encoding the surroundings. Iizuka et al. [20] adopt two discriminators to ensure the inpainted content is both locally and globally consistent. Artifacts can be reduced along the hole boundary by filtering using partial [26] or gated [50] convolutions. Some recent inpainting models improve the generated image quality with additional information, such as edges [30], segmentation masks [40], and low frequency structures [25, 37]. Moreover, several papers show deep neural networks can fill holes on high resolution images [46, 48, 52]. Despite the significant advancements in single inpainting models, filling with one single image remains fundamentally an ill-posed problem [60]. TransFill [62] is closely related to our work: it performs reference-guided inpainting by warping a reference image with multiple homographies. However, due to the planar nature of homographies, TransFill has a limited ability to handle image pairs with complex 3D structures, wide baselines, or significant disocclusions.

Two-view Geometry. SfM establishes correspondences between two monocular frames and subsequently estimates 3D structure. In classic geometric vision, it is well understood that the camera poses as well as the depth maps can be computed from feature matching points alone [27]. Traditional methods utilize hand-crafted descriptors [4, 28, 38]

to build sparse correspondence for the subsequent fundamental matrix estimation with the 8-point algorithm [17]. Learned local features have shown great success in recent works [10, 11, 47] together with the learning-based feature matching models, such as SuperGlue [39] or differentiable formations of RANSAC [6, 7, 35]. Another alternative is to directly estimate relative pose using an end-to-end pose estimation network [21]. We leverage these recent advances (specifically OANet [53]) in our work.

Monocular Depth Estimation. Predicting depth from a single image is an ill-posed problem. However, learning based approaches have shown impressive performance by either treating monocular depth estimation as a regression or classification task [1, 13, 15, 16, 18, 19, 22, 23, 44, 45, 58, 59]. Recent advances include BTS [23], which introduces local planar guidance layers to guide the features to full resolution instead of standard upsampling layers during the decoding phase. DAV [19] proposes to exploit co-planarity of objects in the scene via depth-attention volume. DPT [34] leverages the high quality intermediate representation from transformers and achieves state-of-the-art performance.

3. Method

We assume that we are given a target image $\mathbf{I}_t \in \mathbb{R}^{H_t \times W_t \times 3}$ with a hole indicated by a binary mask $\mathbf{M} \in \mathbb{R}^{H_t \times W_t}$ to be filled, and a reference (source) image $\mathbf{I}_s \in \mathbb{R}^{H_s \times W_s \times 3}$ of the same scene. Our goal is to find a 3D-aware warping $\mathbf{I}_{s \rightarrow t} \in \mathbb{R}^{H_t \times W_t \times 3}$ that geometrically aligns the source image to the target image such that we can use the warped content in $\mathbf{I}_{s \rightarrow t}$ to fill the hole region. We would like the composite image $\mathbf{I}_t^{\text{comp}} = \mathbf{I}_t \odot \mathbf{M} + \mathbf{I}_{s \rightarrow t} \odot (1 - \mathbf{M})$ to be a good estimate for the inpainted result, where \odot represents the element-wise product. In practice we perform refinement and merging to compensate for any residual spatial misalignments or differences in color or exposure. We assume there is significant overlapping content between the source image and target image hole but the overlap region does not necessarily cover the entire hole region.

We establish sparse correspondences between \mathbf{I}_s and \mathbf{I}_t and estimate the relative pose \mathbf{T}_{rel} between two views with the classic 8-point algorithm [17]. Meanwhile, we predict the inverse depth map on the source image using a pre-trained monocular depth estimator: this can be used to estimate the source depth. Mathematically, we only need the source depth and \mathbf{T}_{rel} to compute the 3D-aware warp $\mathbf{I}_{s \rightarrow t}$. However, the source depth is predicted up to an unknown scale and offset by a pre-trained deep model, therefore, we solve for these such that the initial source depth \mathbf{D}_s^i best matches a sparse 3D triangulation: this forms the initial depth estimate shown in Figure 2. Next, we jointly optimize the relative pose and a scale and offset for the depth map to improve the accuracy of relative poses and depth predictions due to potential errors in matching and depth pre-

dictions. Our final $\mathbf{I}_{s \rightarrow t}$ is computed by rendering the textured mesh using the optimized depth predictions and relative camera poses. Similar to TransFill, our approach handles non-overlapping and disoccluded regions in the hole with a state-of-the-art single image inpainting model. We will describe the details of each step in the following sections.

3.1. Estimating Initial Pose and Depth

3.1.1 Computing Initial Relative Pose

As mentioned before, our approach estimates the relative pose \mathbf{T}_{rel} based on predicted sparse correspondences. We extract SIFT features [29] and feed them into OANet [53] to reject outliers and establish correspondences. OANet efficiently predicts a set of points \mathbf{P}_s in the source image and corresponding points \mathbf{P}_t in the target image. Using the OANet correspondences, we compute the fundamental matrix \mathbf{F} between \mathbf{I}_s and \mathbf{I}_t via the normalized 8-point algorithm [17] using RANSAC [14]. From the estimated fundamental matrix \mathbf{F} , we derive the relative pose \mathbf{T}_{rel} using the classic multi-view geometry algorithm mentioned in [17]. Note the estimated translation in \mathbf{T}_{rel} is normalized and will not match the arbitrary scale in the predicted depth maps from pretrained deep models.

3.1.2 Aligning Scale between Relative Pose and Monocular Depth

Admittedly, it is possible to rescale the relative pose to match the depth prediction. However, as suggested in [57], aligning dense depth to sparse triangulated points is much simpler. We first triangulate points with the relative pose, then align the scale of depth predictions with triangulation to subsequently match the scale of the relative pose. Specifically, a 3D triangulated point \mathbf{x} with point $q_s \in \mathbf{P}_s$ and $q_t \in \mathbf{P}_t$ is computed as:

$$\mathbf{x}^* = \underset{\mathbf{x}}{\operatorname{argmin}} [E(\mathbf{r}_s, \mathbf{x})]^2 + [E(\mathbf{r}_t, \mathbf{x})]^2, \quad (1)$$

where \mathbf{r}_s represents the ray shooting from the source camera center through the point q_s on the image plane, \mathbf{r}_t is the ray from the target camera following a similar analogy, and E measures the Euclidean distance between two inputs. In this way, we compute a set of 3D triangulated points \mathbf{X} using all matching sparse correspondences. In order to form the linear problem to compute the scale and offset, we first compute a sparse triangulated depth map \mathbf{D}_{tri} by projecting 3D triangulated points to source camera coordinates. Mathematically, for any triangulated point $\mathbf{x} \in \mathbf{X}$, the corresponding pixel coordinate in \mathbf{D}_{tri} is computed as $\vee(\mathbf{K} \mathbf{x})$, where $\mathbf{K} \in \mathbb{R}^{3 \times 3}$ is the intrinsic matrix and we define the operator $\vee([x, y, z]) = [x/z, y/z]$ that maps from 3D homogeneous coordinates to 2D. We discuss the fixed intrinsic matrix that we use later in implementation details. Note

\mathbf{D}_{tri} is in the same scale as the relative pose. Therefore, we correct \mathbf{D}_s to match \mathbf{D}_{tri} , which subsequently matches the scale of the relative pose. We correct \mathbf{D}_s by estimating two scalars, the scale s^i and offset b^i associated with the depth map, by solving a linear least square problem. The initial depth maps are then expressed as: $\mathbf{D}_s^i = s^i \mathbf{D}_s + b^i$.

3.2. Jointly Optimizing Depth and Pose

To mitigate the effects of potential errors in sparse correspondence and depth estimation, we further introduce an optimization module to improve the quality of $\mathbf{I}_{s \rightarrow t}$. We optimize the depth scale, offset, and the relative pose that jointly define $\mathbf{I}_{s \rightarrow t}$ in the 3D scene. Specifically, we convert the rotation matrix into quaternions, which leads to a total of 9 parameters to optimize. Both relative pose and the initial depth estimate computed in the previous section are used as the initial guess for the optimization. Our optimization contains 3 different loss functions: a multiscale photometric loss, a feature correspondence loss, and a negative depth penalty.

Multiscale photometric loss measures the pixel-level color difference between $\mathbf{I}_{s \rightarrow t}$ and the \mathbf{I}_t outside the hole region. We downsample both $\mathbf{I}_{s \rightarrow t}$ and \mathbf{I}_t and sum the normalized color difference across different resolutions. Specifically, we build Gaussian pyramids on both $\mathbf{I}_{s \rightarrow t}$ and \mathbf{I}_t using an RGB representation for the source image and an alpha-premultiplied RGBA representation on the target image to incorporate the hole region properly into the target image. Computing a multi-scale photometric loss within each iteration is obviously computational expensive. Moreover, the optimization might also get trapped into the local minima associated with the finest resolution due to poor initialization [63]. To accelerate the computation speed and find better solutions, we adopt a coarse-to-fine optimization strategy, which means we first compute photometric loss on the most coarse level and move to the finer level once the convergence criteria at the current pyramid level are met. Additionally, instead of building a 3D triangle mesh and rendering from the target view at each iteration, we use a much more efficient differentiable 3D reprojection to find a warping field that computes $\mathbf{I}_{s \rightarrow t}$ from \mathbf{I}_s with bilinear interpolation. Mathematically, we have:

$$\mathbf{I}_{s \rightarrow t} = \text{bilinear}(\mathbf{I}_s, \text{reproj}(\mathbf{K}, \mathbf{T}_{\text{rel}}, \mathbf{D}_s^o)), \quad (2)$$

where $\text{reproj}()$ represents the 3D reprojection operation. Specifically, for each pixel coordinate p_s in the optimized depth $\mathbf{D}_s^o = s^o \mathbf{D}_s + b^o$, the reprojection finds the corresponding location in the target image coordinate by computing $\vee(\mathbf{K} \mathbf{T}_{\text{rel}} \wedge (\mathbf{D}_s^o(p_s) \mathbf{K}^{-1} p_s^h))$, where $\wedge(u)$ indicates to increase the dimension of u by one by concatenating a 1 to the end, $p_s^h = \wedge(p_s)$ is the homogeneous representation of p_s , and \mathbf{T}_{rel} uses the 3x4 matrix representation. After performing a pixel-wise division through by alpha to re-

cover non-alpha-premultiplied colors, the photometric loss at a given resolution with the pyramid is:

$$l_{\text{photo}} = \frac{1}{|\mathbf{M}|} \sum \mathbf{W} \odot \|\mathbf{I}_{s \rightarrow t} \odot \mathbf{M} - \mathbf{I}_t \odot \mathbf{M}\|^2. \quad (3)$$

Here \mathbf{W} is a pixel importance weight map discussed shortly. We also applied an additional color correction mechanism of the gain and bias from Darabi et al. [9] to slightly compensate for the potential change in auto exposure and lighting conditions between source and target images. We give more details regarding the computation of the loss and the reprojection in the supplemental.

Feature correspondence loss computes the distance between reprojected matching feature points in the source images and the target images. We use the $\text{reproj}()$ operator on all 2D image coordinates in \mathbf{P}_s to get another set $\mathbf{P}_{s \rightarrow t}$. Then, we compute the average distance between $\mathbf{P}_{s \rightarrow t}$ and \mathbf{P}_t . However, the average distance of all points is very sensitive to outliers, i.e., very few outliers dominate the loss function. To reduce the effects of the outliers on the loss function, we adopt the general robust loss function from [3]. The general form of the loss function is:

$$f(x, \alpha, c) = \frac{|\alpha - 2|}{\alpha} \left(\left(\frac{(x/c)^2}{|\alpha - 2|} + 1 \right)^{\alpha/2} - 1 \right), \quad (4)$$

where α and c are the shape and scale parameters, respectively. In our experiments, we set $\alpha = -2$ and $c = 10$. Then, feature correspondence loss is written as:

$$l_{\text{feat}} = \frac{1}{|P_{s \rightarrow t}|} \sum_{i=0}^{|P_{s \rightarrow t}|} \mathbf{W}(\mathbf{q}_t^i) f(\|\mathbf{q}_{s \rightarrow t}^i - \mathbf{q}_t^i\|, \alpha, c), \quad (5)$$

where f is the general robust loss function, $\mathbf{q}_{s \rightarrow t}^i$ and \mathbf{q}_t^i is the i^{th} point in $P_{s \rightarrow t}$ and P_t , respectively.

Negative depth penalty aims to penalize negative values in the remapped depth. Although depth predictions have arbitrary scale and offset, they should have all positive values, meaning that a fragment of geometry associated with a pixel should never move behind the camera. Mathematically, we adopt a hinge loss function:

$$l_{\text{neg}} = \sum \max\{0, -\mathbf{D}_s^o\}. \quad (6)$$

Our final objective function is written as: $l = \lambda_1 l_{\text{neg}} + \lambda_2 l_{\text{photo}} + \lambda_3 l_{\text{feat}}$, where $\{\lambda_j\}$ are weights for loss terms.

A **pixel importance weight map** is proposed to help our optimization better align the warped source image with the target image both locally and globally. When computing the photometric loss or feature correspondence loss, we assign weights to each pixel instead of a uniform weighting. The first type of weighting strategy is hole-based weighting. We first compute a distance map \mathbf{M}_h with the distance transform to find the Euclidean distance of each pixel

to the closest boundary pixel of the hole M_h . We compute the weight at each pixel using a Gaussian function based on M_h . The pixel-level hole-based weighting map $\mathbf{W}_h = \exp(-M_h^2/2\sigma^2)$, where σ is a hyperparameter that adjusts how weights change w.r.t distance to the hole boundary. The intuition behind this weight map is to have the optimization focus on the regions close to the hole since those pixels are later used to fill the hole regions. The second type of weighting strategy is the edge-based weighting. We compute a multi-scale Canny edge map by first applying Gaussian blur on \mathbf{I}_t with N different kernel sizes, run the Canny edge detector [8] on each image, and dilate each edge to get $\{e_1, e_2, \dots, e_N\}$. Our pixel-level edge-based weight map $\mathbf{W}_e = \sum_{i=1}^N e_i / \sum_p e_i(p)$, where the inner sum is over spatial coordinates. By computing Canny edge maps with different kernel sizes and summing over multiple normalized edge maps, we intend to give strong edges larger weights. Our overall weighting $\mathbf{W} = \mathbf{W}_h \odot \mathbf{W}_e$.

3.3. Final Rendering and Postprocessing

Mesh rendering. From the optimization module, we find $\mathbf{T}_{\text{rel}}^o$, s^o , and b^o . However, computing $\mathbf{I}_{s \rightarrow t}$ using depth reprojection always has some gaps between valid pixels due to it relying on a forward warping for efficiency in the inner loop of the optimization. One way to overcome this problem is interpolation but that has two disadvantages. First, the reprojected image is sparse and for regions with multiple layers of depth, pixels for a far-away depth layer might splat between pixels of a closer depth layer, which could result in interpolations that do not fully remove hidden surfaces. Additionally, interpolation cannot distinguish between holes due to disoccluded regions or simple gaps between the pixels due to the forward warping.

Due to the problems mentioned above, we choose to render a textured mesh to get the final $\mathbf{I}_{s \rightarrow t}$. We first build a triangle mesh with a regular grid from the source view. The mesh vertices are computed by projecting the optimized depth \mathbf{D}_s^o to the 3D space and the texture is the RGB colors of the source image. After building the triangle mesh, we drop the edges around depth discontinuities. We adopt a simplified version of the footprint algorithm [41] by comparing the depth values between connected vertices. We drop the edge between two vertices v_i and v_j if

$$\frac{2|d(v_i) - d(v_j)|}{d(v_i) + d(v_j)} > \epsilon_{\text{edge}}, \quad (7)$$

where $d(v_i)$ is the depth value of the vertex v_i and ϵ_{edge} is a predefined threshold. After building the triangle mesh, we render the target view with $\mathbf{T}_{\text{rel}}^o$. Note that we also normalize the mesh to the unit size before rendering. We use PyTorch3D [36] as our renderer. The textured mesh densely fills in pixels and removes hidden surfaces. It also allows us to use the rendered alpha channel to find places where

there is no intersection with the mesh, which represent disoccluded regions near depth discontinuities or regions outside the photo: these are later filled by single image inpainting.

Refinement and Merging. With the rendered image, we apply the color-spatial transformation (CST) module from TransFill to further improve any small residual spatial misalignments and correct color and exposure differences. Lastly, we merge the output from CST with results from the single image inpainting model as in TransFill to handle the disocclusions and regions outside the photo.

4. Experiments

Datasets. We first evaluate GeoFill and other baselines on the RealEstate10K [61] dataset, which contains a diverse collection of YouTube video sequences shot from a moving camera for both indoor and outdoor scenes. Each video clip contains a variety of views of the same scene. We randomly sample 500 videos and select one pair of images in each video sequence with a specific frame difference (FD). Specifically, we sample FD=25, 50, and 75 to build three different sets with a resolution of 720×1280 while automatically filtering out image pairs without enough overlap inside the hole by checking the number of matching sparse features. We follow DeepFillv2 [50] to generate random free-form brush stroke masks.

Additionally, we also evaluate all approaches on the MannequinChallenge [24] dataset. This is a challenging dataset with video sequences shot from a hand-held camera freely roaming in a scene of people with frozen poses. This dataset contains more than 170K frames and corresponding camera poses derived from about 2k YouTube videos. The camera motion in this dataset is more extreme and scene complexity is much higher due to diverse frozen human poses and rich background objects. We reduce the sampling FD to ensure enough overlap between image pairs. Similar to the previous dataset, we randomly sample 3 subsets with FD=10, 20, 30, where each contains 500 image pairs with resolution of 720×1280 after filtering.

Baselines. In addition to TransFill, which is directly related to our work, we compare our approach against several different types of baselines. The first type is state-of-the-art video completion models. OPN [31] achieves high quality inpainting results with spatio-temporal attention. STTN [51] proposes filling holes by optimizing a spatial-temporal adversarial loss function. In addition, we compare against state-of-the-art single-image inpainting methods. ProFill [52] utilizes a contextual attention module and progressively fills the hole with predicted high-confidence pixels. CoModGAN [56] proposes a co-modulation of both conditional and stochastic representations to fill high quality content. Lastly, we compare a two-view SfM based approach [57] — which we refer to as JointDP — by warping

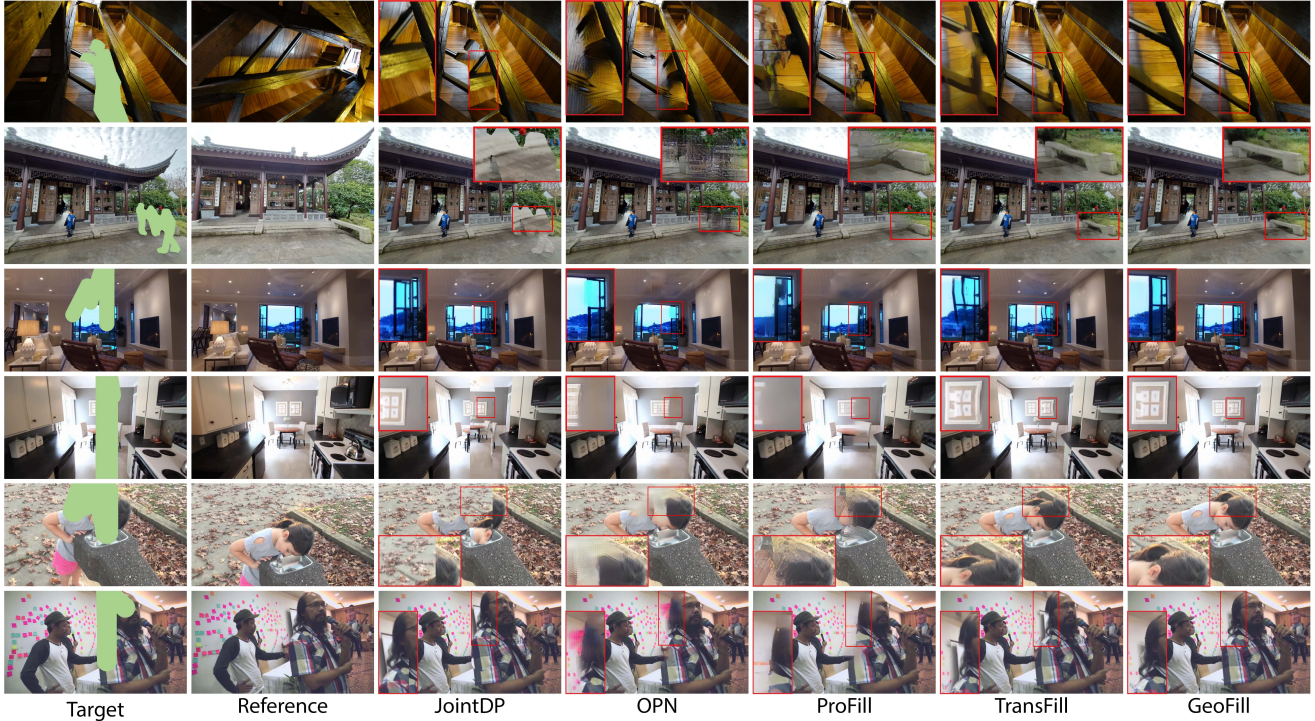


Figure 3. Qualitatively comparison of GeoFill against other baselines on user-provided images (top 2 rows), RealEstate10K (mid 2 rows), and MannequinChallenge dataset (last two rows).

the source image with the jointly estimated relative pose and depth using dense correspondence. To ensure fairness in the comparison, we also warp the image by building a triangle mesh and rendering it with the predicted relative pose while keeping all other settings the same.

Implementation Details. We use pretrained OANet [53] and SIFT [29] for correspondence matching and outlier rejection. Our pretrained monocular depth predictor is DPT [34]. We use fixed camera intrinsic parameters for all images by setting the focal length to 750 and the principal point to the center of the image. Our pipeline is implemented with PyTorch [32] and we choose DiffGrad [12] as our optimizer due to its fast convergence speed. In the optimization step, we use a constant learning rate 10^{-2} and the maximum number of iteration is set to 10^4 . The loss weights λ_1 , λ_2 , and λ_3 are 10, 10, 0.5, respectively. In the coarse-to-fine optimization strategy, the number of pyramid levels is 4 and the maximum number of cumulative iterations at each level from coarse to fine are 4×10^3 , 7×10^3 , 9×10^3 , 10^4 . We set the σ in hole-based weighting to 192 pixels. In edge-based weight, we compute 4 different Canny edge maps and dilate each of them with a kernel size equal to 4. In mesh rendering, the edge threshold ϵ_{edge} is 4×10^{-2} .

4.1. Quantitative Results

The quantitative results comparing our approach with other baselines are shown in Table 1. We report the PSNR,

SSIM and LPIPS [55] on the RealEstate10K and the MannequinChallenge datasets. Neither single image inpainting models are competitive for image pairs with larger scale differences and wider baselines. We believe CoModGAN performs worse since it sometimes tries to hallucinate different objects and structures that are consistent with the GAN loss instead of matching the content in the target images. Video completion approaches also show bad performance due to the lack of temporal information. JointDP is based on optical flow and is not able to accurately estimate parameters like the camera pose needed to correctly align the image pairs. Our method demonstrates superiority over TransFill because we have a better understanding of the 3D structures of the scenes, and better leverage the depth estimation. Additionally, we only have a single proposal to merge during inpainting, which greatly reduces blending artifacts that arise from multiple proposals. Therefore, our GeoFill is robust and stable on image pairs with even larger frame differences.

4.2. Qualitative Results

Figure 3 shows the visual comparisons with other baseline algorithms on the user-provided images, the RealEstate10K and the MannequinChallenge dataset. JointDP utilizes estimated optical flow for the initial matching, thus the results fail to obtain accurate depth and camera pose if the baseline of the image pair is wide. The contents

Table 1. Quantitative comparisons of GeoFill against other baselines on both RealEstate10K and MannequinChallenge datasets.

Model	RealEstate10K: PSNR ↑ / SSIM ↑ / LPIPS ↓			MannequinChallenge: PSNR ↑ / SSIM ↑ / LPIPS ↓		
	FD=25	FD=50	FD=75	FD=10	FD=20	FD=30
JointDP [57]	22.46 / 0.9469 / 0.1011	21.76 / 0.9457 / 0.1063	20.89 / 0.9423 / 0.1122	20.13 / 0.9346 / 0.1087	19.52 / 0.9290 / 0.1195	19.38 / 0.9315 / 0.1177
OPN [31]	28.41 / 0.9684 / 0.0525	27.80 / 0.9669 / 0.0570	26.91 / 0.9634 / 0.0624	25.63 / 0.9628 / 0.0605	24.92 / 0.9584 / 0.0698	24.84 / 0.9591 / 0.0702
STTN [51]	28.83 / 0.9696 / 0.0710	28.26 / 0.9697 / 0.0721	27.59 / 0.9680 / 0.0751	25.60 / 0.9623 / 0.0803	25.09 / 0.9602 / 0.0865	24.94 / 0.9613 / 0.0844
ProFill [52]	27.45 / 0.9642 / 0.0775	27.67 / 0.9654 / 0.0755	27.37 / 0.9639 / 0.0768	25.04 / 0.9589 / 0.0808	25.02 / 0.9582 / 0.0836	25.22 / 0.9599 / 0.0810
CoModGAN [56]	26.02 / 0.9594 / 0.0703	26.14 / 0.9607 / 0.0686	25.88 / 0.9596 / 0.0697	23.39 / 0.9504 / 0.0770	23.14 / 0.9486 / 0.0808	23.36 / 0.9503 / 0.0791
TransFill [62]	32.03 / 0.9764 / 0.0461	30.64 / 0.9732 / 0.0540	29.24 / 0.9694 / 0.0608	28.01 / 0.9680 / 0.0569	26.56 / 0.9628 / 0.0688	26.17 / 0.9632 / 0.0701
GeoFill (Ours)	32.57 / 0.9775 / 0.0467	31.47 / 0.9748 / 0.0525	30.43 / 0.9717 / 0.0581	28.85 / 0.9702 / 0.0553	27.72 / 0.9658 / 0.0652	27.44 / 0.9664 / 0.0665

Table 2. Quantitative comparisons of GeoFill using different combinations of terms in the joint optimization objective.

Photo	Feat	NegD	PSNR↑	SSIM↑	LPIPS↓
✓	✓	✓	31.47	0.9748	0.0525
✗	✓	✓	31.19	0.9742	0.0533
✓	✗	✓	30.88	0.9734	0.0554
✓	✓	✗	31.23	0.9742	0.0532

inside the hole are often misaligned with the target image. The original OPN uses five reference frames to achieve a more efficient non-local matching among frames, but a single reference frame makes the results non-realistic. ProFill is not able to take advantage of the reference image contents, and TransFill usually has blending artifacts or content misalignment issues when objects inside the hole regions occupy multiple depth planes. However, our proposed GeoFill avoids the blending artifacts by using one single proposal, and aligns the objects well by understanding the camera poses and reconstructing the 3D scene from two images.

4.3. Ablation Study

In the following sections, we study how each optimization loss function and the pixel importance weight maps contribute to the final results. Additionally, we present experimental results of TransFill and GeoFill on cases with larger holes and their alignment accuracy without CST. All experiment results in the following section are reported for the RealEstate10K FD=50 subset unless specified.

Optimization objective functions. To characterize how each term in the objective function contributes to the optimization results, we run our approach with different objective functions. Specifically, we check how our model performance changes after removing one of the terms, as shown in Table 2. Comparing GeoFill without photometric loss against without feature correspondence loss, the feature loss contributes to the performance the most because the model without it has the worst performance among all comparisons. We find that photometric loss by itself may get distracted by local textures and fall into local minima, such that it achieves lower RGB errors on average but ignores the global structure. However, using the photometric loss does help improve alignments. Lastly, GeoFill without negative depth penalty still has a performance drop, suggesting negative depth penalty is able to prevent corner cases where depth scale or offset are extremely wrong.

Table 3. Initial alignment comparisons of our method compared to TransFill without the CST Module.

Model	PSNR↑	SSIM↑	LPIPS↓
GeoFill	31.47	0.9748	0.0525
GeoFill (no CST)	29.35	0.9688	0.0579
TransFill	30.64	0.9732	0.0540
TransFill (no CST)	26.03	0.9598	0.0742

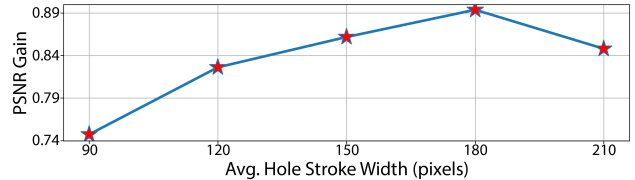


Figure 4. Performance gain of our method compared to TransFill w.r.t the average hole size.

Performance w.r.t hole size. This ablation study aims to examine the performance of our approach against TransFill under more difficult settings. As the hole becomes larger, inevitably we have fewer matching points, which makes $I_{s \rightarrow t}$ hard to align with I_t . We generate holes with different average stroke widths ranging from 90 to 210 pixels. Note that we fix the random seed such that holes in different sets still have the same shape for a fair comparison. As shown in Figure 4, GeoFill has an increasing performance gain over TransFill until the hole average stroke width reaches 180 pixels. As the hole size grows, the complexity of the content in the hole also increases. In other words, we are more likely to encounter a growing number of depth layers, a more complicated objects layout, and a higher chance of occlusions due to camera translation in a larger hole. These problems are harder for homography-based models, therefore, GeoFill has a greater advantage when the hole is larger. The reason that we observe a drop in performance gain at the end of the curve is that there are not enough matching points for GeoFill to infer as accurate of a 3D structure.

Initial alignment comparisons against TransFill. We adopted the CST module from TransFill to adjust auto exposure, lighting conditions, and potential remaining misalignments. In this experiment, we analyze the performance of using the aligned images directly, e.g. without using CST for both models. We retain the multiple homographies used by TransFill, drop the CST module, and keep the merging module so TransFill can merge its different regions. As

Table 4. Quantitative comparisons of GeoFill with different pixel importance weight maps in the optimization.

Hole	Edge	PSNR \uparrow	SSIM \uparrow	LPIPS \downarrow
✓	✓	31.47	0.9748	0.0525
✓	✗	31.20	0.9740	0.0534
✗	✓	31.12	0.9739	0.0539
✗	✗	30.95	0.9734	0.0552

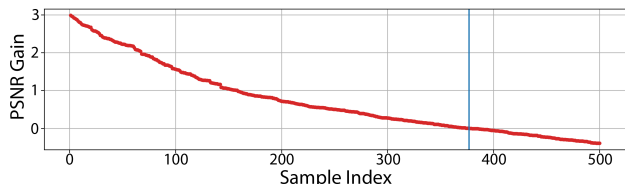


Figure 5. Per-sample performance gain of ours compared to TransFill. The blue vertical line represents the index separating positive and negative PSNR gain.

shown in Table 3, GeoFill maintains better performance, dropping 2.12 in PSNR, while TransFill drops 4.62 without CST. This experimentally validates the proposal from GeoFill is much more accurate than TransFill by better leveraging the depth information.

Pixel importance weight map in the optimization. We present results of GeoFill with different combinations of pixel importance weight maps in the optimization in Table 4. Comparing between hole-based weighting and edge-based weighting, hole-base weighting has a slight advantage. Hole-based weight maps put higher weights around the hole and lead to better local alignment around the hole. Edge-based weighting attempts to match strong edges within the entire image. Therefore, the optimized results have lower average quantitative performance. Lastly, using a uniform weighting map leads to the worst performance, indicating the effectiveness of the weighting maps.

Per-sample improvement study. This ablation is designed to break down the numbers shown in Table 1 by comparing the performance of GeoFill against TransFill over each individual sample. We sort and plot the per-image PSNR difference over TransFill, shown in Figure 5. Specifically, PSNR difference is computed as GeoFill PSNR – TransFill PSNR, therefore a positive PSNR gain indicates GeoFill is better. GeoFill improves performance on the majority of samples, specifically for around 75.4% of the entire subset. Moreover, the PSNR gains when GeoFill outperforms are much greater: up to 3 dB, as opposed to the PSNR losses when TransFill outperforms.

5. Discussion, Limitations, and Conclusion

Limitations and future work. GeoFill inpaints the hole with one image pair with no auxiliary pose or depth information from sensors, therefore, our pipeline may not work well when the quality of feature matching points is poor,

e.g., matching points are inaccurate or too few. Under these cases, our relative pose and triangulated points can be inaccurate, which may be hard for optimization to correct. Additionally, our pipeline is also sensitive to depth prediction quality: artifacts such as blurry depth discontinuities or wrong order of depth planes can lead to potential bad inpainting results. Future work might mitigate these problems by jointly reasoning about monocular depth and the stereo cues established by triangulation. In the optimization, we used a 3D reprojection based on forward warping because it is much faster than rendering a triangle mesh even though it does not fully remove hidden surfaces in the rare cases where a mesh occludes itself: this could be addressed in future work by testing and pruning those splatted points. GeoFill utilizes the CST module to adjust auto exposure and lighting condition changes, which still suffers when the scene environment changes drastically, e.g., day to night, spring to fall. Future work could better address these by incorporating specialized lighting estimation (e.g., [54]) and relighting modules. One last limitation of GeoFill is that our pipeline only handles static scenes. Any dynamic objects, e.g., walking people or moving cars, not in the hole could lead to bad relative pose estimation and our optimization may cause misalignments under such cases. A simple solution would be masking out objects that are likely to move such as people and cars, but how to correctly identify all moving objects is still an open question.

Potential negative impact. The goal of image inpainting research is to generate realistic image contents while removing or changing contents of the photos. We believe that there can be scenarios where our model is misused. Countermeasures against the falsification of images may include both technical measures and legal measures. Technical measures include developing additional discriminators or watermark for decoders to recognize. Legal measures include the draft U.S. bill H.R. 3230, which requires users to mark the images which are digitally modified. One could use both to mitigate the ethical issues.

Conclusion. In this work, we proposed a novel reference-based inpainting approach that achieves state-of-the-art performance. Our method relies on off-the-shelf depth estimation and sparse correspondence methods, and thus we can expect its performance to improve if these modules improve in performance. Compared to previous homography-based work, GeoFill is better at image pairs with large camera motions and scenes with complicated structures in the hole. GeoFill ensures accurate alignment between the filling content and the hole by jointly optimizing depth predictions and relative poses without explicitly knowing camera intrinsic parameters. Moreover, our approach inpaints the hole in a more efficient and principled way by utilizing one single proposal without heuristic planar assumptions.

References

- [1] Ibraheem Alhashim and Peter Wonka. High quality monocular depth estimation via transfer learning. *arXiv preprint arXiv:1812.11941*, 2018. 3
- [2] Connelly Barnes, Eli Shechtman, Adam Finkelstein, and Dan B Goldman. Patchmatch: A randomized correspondence algorithm for structural image editing. *ACM Trans. Graph.*, 28(3):24, 2009. 2
- [3] Jonathan T Barron. A general and adaptive robust loss function. In *Proceedings of the IEEE/CVF Conference on Computer Vision and Pattern Recognition*, pages 4331–4339, 2019. 4
- [4] Herbert Bay, Tinne Tuytelaars, and Luc Van Gool. Surf: Speeded up robust features. In *European conference on computer vision*, pages 404–417. Springer, 2006. 2
- [5] Marcelo Bertalmio, Guillermo Sapiro, Vincent Caselles, and Coloma Ballester. Image inpainting. In *Proceedings of the 27th annual conference on Computer graphics and interactive techniques*, pages 417–424, 2000. 2
- [6] Eric Brachmann, Alexander Krull, Sebastian Nowozin, Jamie Shotton, Frank Michel, Stefan Gumhold, and Carsten Rother. Dsac-differentiable ransac for camera localization. In *Proceedings of the IEEE Conference on Computer Vision and Pattern Recognition*, pages 6684–6692, 2017. 3
- [7] Eric Brachmann and Carsten Rother. Neural-guided ransac: Learning where to sample model hypotheses. In *Proceedings of the IEEE/CVF International Conference on Computer Vision*, pages 4322–4331, 2019. 3
- [8] John Canny. A computational approach to edge detection. *IEEE Transactions on pattern analysis and machine intelligence*, (6):679–698, 1986. 5
- [9] Soheil Darabi, Eli Shechtman, Connelly Barnes, Dan B Goldman, and Pradeep Sen. Image melding: Combining inconsistent images using patch-based synthesis. *ACM Transactions on graphics (TOG)*, 31(4):1–10, 2012. 4
- [10] Daniel DeTone, Tomasz Malisiewicz, and Andrew Rabinovich. Toward geometric deep slam. *arXiv preprint arXiv:1707.07410*, 2017. 3
- [11] Daniel DeTone, Tomasz Malisiewicz, and Andrew Rabinovich. Superpoint: Self-supervised interest point detection and description. In *Proceedings of the IEEE conference on computer vision and pattern recognition workshops*, pages 224–236, 2018. 3
- [12] Shiv Ram Dubey, Soumendu Chakraborty, Swalpa Kumar Roy, Snehasis Mukherjee, Satish Kumar Singh, and Bidyut Baran Chaudhuri. diffgrad: An optimization method for convolutional neural networks. *IEEE transactions on neural networks and learning systems*, 31(11):4500–4511, 2019. 6
- [13] David Eigen, Christian Puhrsch, and Rob Fergus. Depth map prediction from a single image using a multi-scale deep network. *arXiv preprint arXiv:1406.2283*, 2014. 3
- [14] Martin A Fischler and Robert C Bolles. Random sample consensus: a paradigm for model fitting with applications to image analysis and automated cartography. *Communications of the ACM*, 24(6):381–395, 1981. 3
- [15] Huan Fu, Mingming Gong, Chaohui Wang, Kayhan Batmanghelich, and Dacheng Tao. Deep ordinal regression network for monocular depth estimation. In *Proceedings of the IEEE conference on computer vision and pattern recognition*, pages 2002–2011, 2018. 3
- [16] Zhixiang Hao, Yu Li, Shaodi You, and Feng Lu. Detail preserving depth estimation from a single image using attention guided networks. In *2018 International Conference on 3D Vision (3DV)*, pages 304–313. IEEE, 2018. 3
- [17] Richard I Hartley. In defense of the eight-point algorithm. *IEEE Transactions on pattern analysis and machine intelligence*, 19(6):580–593, 1997. 3
- [18] Junjie Hu, Mete Ozay, Yan Zhang, and Takayuki Okatani. Revisiting single image depth estimation: Toward higher resolution maps with accurate object boundaries. In *2019 IEEE Winter Conference on Applications of Computer Vision (WACV)*, pages 1043–1051. IEEE, 2019. 3
- [19] Lam Huynh, Phong Nguyen-Ha, Jiri Matas, Esa Rahtu, and Janne Heikkilä. Guiding monocular depth estimation using depth-attention volume. In *European Conference on Computer Vision*, pages 581–597. Springer, 2020. 3
- [20] Satoshi Iizuka, Edgar Simo-Serra, and Hiroshi Ishikawa. Globally and locally consistent image completion. *ACM Transactions on Graphics (ToG)*, 36(4):1–14, 2017. 2
- [21] Alex Kendall, Matthew Grimes, and Roberto Cipolla. PoseNet: A convolutional network for real-time 6-dof camera relocalization. In *Proceedings of the IEEE international conference on computer vision*, pages 2938–2946, 2015. 3
- [22] Iro Laina, Christian Rupprecht, Vasileios Belagiannis, Federico Tombari, and Nassir Navab. Deeper depth prediction with fully convolutional residual networks. In *2016 Fourth international conference on 3D vision (3DV)*, pages 239–248. IEEE, 2016. 3
- [23] Jin Han Lee, Myung-Kyu Han, Dong Wook Ko, and Il Hong Suh. From big to small: Multi-scale local planar guidance for monocular depth estimation. *arXiv preprint arXiv:1907.10326*, 2019. 3
- [24] Zhengqi Li, Tali Dekel, Forrester Cole, Richard Tucker, Noah Snavely, Ce Liu, and William T Freeman. Learning the depths of moving people by watching frozen people. In *Proceedings of the IEEE/CVF Conference on Computer Vision and Pattern Recognition*, pages 4521–4530, 2019. 5
- [25] Liang Liao, Jing Xiao, Zheng Wang, Chia-Wen Lin, and Shin’ichi Satoh. Guidance and evaluation: Semantic-aware image inpainting for mixed scenes. In *Computer Vision—ECCV 2020: 16th European Conference, Glasgow, UK, August 23–28, 2020, Proceedings, Part XXVII 16*, pages 683–700. Springer, 2020. 2
- [26] Guilin Liu, Fitsum A Reda, Kevin J Shih, Ting-Chun Wang, Andrew Tao, and Bryan Catanzaro. Image inpainting for irregular holes using partial convolutions. In *Proceedings of the European Conference on Computer Vision (ECCV)*, pages 85–100, 2018. 2
- [27] H Christopher Longuet-Higgins. A computer algorithm for reconstructing a scene from two projections. *Nature*, 293(5828):133–135, 1981. 2
- [28] David G Lowe. Object recognition from local scale-invariant features. In *Proceedings of the seventh IEEE international*

- conference on computer vision*, volume 2, pages 1150–1157. Ieee, 1999. 2
- [29] David G Lowe. Distinctive image features from scale-invariant keypoints. *International journal of computer vision*, 60(2):91–110, 2004. 3, 6
- [30] Kamyar Nazeri, Eric Ng, Tony Joseph, Faisal Z Qureshi, and Mehran Ebrahimi. Edgeconnect: Generative image inpainting with adversarial edge learning. *arXiv preprint arXiv:1901.00212*, 2019. 2
- [31] Seoung Wug Oh, Sungho Lee, Joon-Young Lee, and Seon Joo Kim. Onion-peel networks for deep video completion. In *Proceedings of the IEEE/CVF International Conference on Computer Vision*, pages 4403–4412, 2019. 5, 7
- [32] Adam Paszke, Sam Gross, Francisco Massa, Adam Lerer, James Bradbury, Gregory Chanan, Trevor Killeen, Zeming Lin, Natalia Gimelshein, Luca Antiga, et al. Pytorch: An imperative style, high-performance deep learning library. *Advances in neural information processing systems*, 32:8026–8037, 2019. 6
- [33] Deepak Pathak, Philipp Krahenbuhl, Jeff Donahue, Trevor Darrell, and Alexei A Efros. Context encoders: Feature learning by inpainting. In *Proceedings of the IEEE conference on computer vision and pattern recognition*, pages 2536–2544, 2016. 2
- [34] René Ranftl, Alexey Bochkovskiy, and Vladlen Koltun. Vision transformers for dense prediction. In *Proceedings of the IEEE/CVF International Conference on Computer Vision*, pages 12179–12188, 2021. 3, 6
- [35] René Ranftl and Vladlen Koltun. Deep fundamental matrix estimation. In *Proceedings of the European conference on computer vision (ECCV)*, pages 284–299, 2018. 3
- [36] Nikhila Ravi, Jeremy Reizenstein, David Novotny, Taylor Gordon, Wan-Yen Lo, Justin Johnson, and Georgia Gkioxari. Accelerating 3d deep learning with pytorch3d. *arXiv preprint arXiv:2007.08501*, 2020. 5
- [37] Yurui Ren, Xiaoming Yu, Ruonan Zhang, Thomas H Li, Shan Liu, and Ge Li. Structureflow: Image inpainting via structure-aware appearance flow. In *Proceedings of the IEEE/CVF International Conference on Computer Vision*, pages 181–190, 2019. 2
- [38] Ethan Rublee, Vincent Rabaud, Kurt Konolige, and Gary Bradski. Orb: An efficient alternative to sift or surf. In *2011 International conference on computer vision*, pages 2564–2571. Ieee, 2011. 2
- [39] Paul-Edouard Sarlin, Daniel DeTone, Tomasz Malisiewicz, and Andrew Rabinovich. Superglue: Learning feature matching with graph neural networks. In *Proceedings of the IEEE/CVF conference on computer vision and pattern recognition*, pages 4938–4947, 2020. 3
- [40] Yuhang Song, Chao Yang, Yeji Shen, Peng Wang, Qin Huang, and C-C Jay Kuo. Spg-net: Segmentation prediction and guidance network for image inpainting. *arXiv preprint arXiv:1805.03356*, 2018. 2
- [41] Lee Westover. Footprint evaluation for volume rendering. In *Proceedings of the 17th annual conference on Computer graphics and interactive techniques*, pages 367–376, 1990. 5
- [42] Yonatan Wexler, Eli Shechtman, and Michal Irani. Space-time video completion. In *Proceedings of the 2004 IEEE Computer Society Conference on Computer Vision and Pattern Recognition, 2004. CVPR 2004.*, volume 1, pages I–I. IEEE, 2004. 2
- [43] Wei Xiong, Jiahui Yu, Zhe Lin, Jimei Yang, Xin Lu, Connelly Barnes, and Jiebo Luo. Foreground-aware image inpainting. In *Proceedings of the IEEE/CVF Conference on Computer Vision and Pattern Recognition*, pages 5840–5848, 2019. 1
- [44] Dan Xu, Elisa Ricci, Wanli Ouyang, Xiaogang Wang, and Nicu Sebe. Multi-scale continuous crfs as sequential deep networks for monocular depth estimation. In *Proceedings of the IEEE conference on computer vision and pattern recognition*, pages 5354–5362, 2017. 3
- [45] Dan Xu, Wei Wang, Hao Tang, Hong Liu, Nicu Sebe, and Elisa Ricci. Structured attention guided convolutional neural fields for monocular depth estimation. In *Proceedings of the IEEE conference on computer vision and pattern recognition*, pages 3917–3925, 2018. 3
- [46] Chao Yang, Xin Lu, Zhe Lin, Eli Shechtman, Oliver Wang, and Hao Li. High-resolution image inpainting using multi-scale neural patch synthesis. In *Proceedings of the IEEE conference on computer vision and pattern recognition*, pages 6721–6729, 2017. 2
- [47] Kwang Moo Yi, Eduard Trulls, Vincent Lepetit, and Pascal Fua. Lift: Learned invariant feature transform. In *European conference on computer vision*, pages 467–483. Springer, 2016. 3
- [48] Zili Yi, Qiang Tang, Shekoofeh Azizi, Daesik Jang, and Zhan Xu. Contextual residual aggregation for ultra high-resolution image inpainting. In *Proceedings of the IEEE/CVF Conference on Computer Vision and Pattern Recognition*, pages 7508–7517, 2020. 2
- [49] Jiahui Yu, Zhe Lin, Jimei Yang, Xiaohui Shen, Xin Lu, and Thomas S Huang. Generative image inpainting with contextual attention. In *Proceedings of the IEEE conference on computer vision and pattern recognition*, pages 5505–5514, 2018. 1
- [50] Jiahui Yu, Zhe Lin, Jimei Yang, Xiaohui Shen, Xin Lu, and Thomas S Huang. Free-form image inpainting with gated convolution. In *Proceedings of the IEEE/CVF International Conference on Computer Vision*, pages 4471–4480, 2019. 1, 2, 5
- [51] Yanhong Zeng, Jianlong Fu, and title = Learning Joint Spatial-Temporal Transformations for Video Inpainting booktitle = The Proceedings of the European Conference on Computer Vision (ECCV) year = 2020 Chao, Hongyang. 5, 7
- [52] Yu Zeng, Zhe Lin, Jimei Yang, Jianming Zhang, Eli Shechtman, and Huchuan Lu. High-resolution image inpainting with iterative confidence feedback and guided upsampling. In *European Conference on Computer Vision*, pages 1–17. Springer, 2020. 2, 5, 7
- [53] Jiahui Zhang, Dawei Sun, Zixin Luo, Anbang Yao, Lei Zhou, Tianwei Shen, Yurong Chen, Long Quan, and Hongen Liao. Learning two-view correspondences and geometry using order-aware network. In *Proceedings of the IEEE/CVF International Conference on Computer Vision*, pages 5845–5854, 2019. 3, 6

- [54] Jinsong Zhang, Kalyan Sunkavalli, Yannick Hold-Geoffroy, Sunil Hadap, Jonathan Eisenman, and Jean-François Lalonde. All-weather deep outdoor lighting estimation. In *Proceedings of the IEEE/CVF Conference on Computer Vision and Pattern Recognition*, pages 10158–10166, 2019. 8
- [55] Richard Zhang, Phillip Isola, Alexei A Efros, Eli Shechtman, and Oliver Wang. The unreasonable effectiveness of deep features as a perceptual metric. In *CVPR*, 2018. 6
- [56] Shengyu Zhao, Jonathan Cui, Yilun Sheng, Yue Dong, Xiao Liang, Eric I Chang, and Yan Xu. Large scale image completion via co-modulated generative adversarial networks. *arXiv preprint arXiv:2103.10428*, 2021. 5, 7
- [57] Wang Zhao, Shaohui Liu, Yezhi Shu, and Yong-Jin Liu. Towards better generalization: Joint depth-pose learning without posenet. In *Proceedings of the IEEE/CVF Conference on Computer Vision and Pattern Recognition*, pages 9151–9161, 2020. 3, 5, 7
- [58] Yunhan Zhao, Shu Kong, and Charless Fowlkes. Camera pose matters: Improving depth prediction by mitigating pose distribution bias. In *Proceedings of the IEEE/CVF Conference on Computer Vision and Pattern Recognition*, pages 15759–15768, 2021. 3
- [59] Yunhan Zhao, Shu Kong, Daeyun Shin, and Charless Fowlkes. Domain decluttering: Simplifying images to mitigate synthetic-real domain shift and improve depth estimation. In *Proceedings of the IEEE/CVF Conference on Computer Vision and Pattern Recognition*, pages 3330–3340, 2020. 3
- [60] Chuanxia Zheng, Tat-Jen Cham, and Jianfei Cai. Pluralistic image completion. In *Proceedings of the IEEE/CVF Conference on Computer Vision and Pattern Recognition*, pages 1438–1447, 2019. 2
- [61] Tinghui Zhou, Richard Tucker, John Flynn, Graham Fyffe, and Noah Snavely. Stereo magnification: Learning view synthesis using multiplane images. *arXiv preprint arXiv:1805.09817*, 2018. 5
- [62] Yuqian Zhou, Connelly Barnes, Eli Shechtman, and Sohrab Amirghodsi. Transfill: Reference-guided image inpainting by merging multiple color and spatial transformations. In *Proceedings of the IEEE/CVF Conference on Computer Vision and Pattern Recognition*, pages 2266–2276, 2021. 1, 2, 7
- [63] Shizhan Zhu, Cheng Li, Chen Change Loy, and Xiaoou Tang. Face alignment by coarse-to-fine shape searching. In *Proceedings of the IEEE conference on computer vision and pattern recognition*, pages 4998–5006, 2015. 4

Appendices

In the supplementary document, we provide additional ablation studies to further support our findings, as well as details of our experiments and more visualizations. Below is the outline.

- **Section A: Convergence criteria in optimization.** We describe the convergence criteria of our optimization in details.
- **Section B: Initial Guess vs Optimized Performance.** We present quantitative comparisons of GeoFill with initial estimated parameters and optimized parameters.
- **Section C: Performance w.r.t intrinsic parameters.** Quantitative comparisons of our approach with different focal lengths.
- **Section D: Visualizations of hole ablation study.** We provide qualitative comparisons between GeoFill and TransFill under various hole sizes.
- **Section E: Visualizations of initial alignments without CST.** Alignment visualizations of GeoFill and TransFill without the CST module.
- **Section F: User study against other baselines.** User study of GeoFill against OPN, ProFill, and TransFill.
- **Section G: Failure cases.** Visual examples of failures cases of GeoFill.
- **Additional Visual Results.** We include more inpainting results in Figure 10 and 11.

A. Convergence Criteria in Optimization

The convergence criteria define a point at which the optimization stops. Our optimization halts the loop at a given scale and continues to the next scale if the following condition is met or the predefined maximum number of iteration is achieved. The formula below measures the objective function value changes within the last m iterations.

$$\epsilon_i = \frac{|\sum_{i-(m/2)-1}^i l_i - \sum_{i-m-1}^{i-m} l_i|}{\sum_{i-(m/2)-1}^i l_i}, \quad (8)$$

where i represents the i^{th} iteration. If ϵ_i is smaller than a predefined ϵ_{opt} , we assume the final objective function converges. Since we adopt a coarse-to-fine optimization strategy, we check the same condition at every level of the pyramid. In other words, we move to the finer scale level only if Eqn. 8 is met or maximum number of iterations at the current level is reached. We also keep track of the optimal parameters at each level and use them as the initialization in the next level. In practice, we set the convergence threshold ϵ_{opt} to 1e-6 for all levels. The number of loss values to track in computing convergence criteria is 10.

Table 5. Quantitative comparison of our method with initial estimated parameters and optimized parameters.

Model	PSNR \uparrow	SSIM \uparrow	LPIPS \downarrow
GeoFill (optim)	31.47	0.9748	0.0525
GeoFill (init)	30.66	0.9719	0.0548

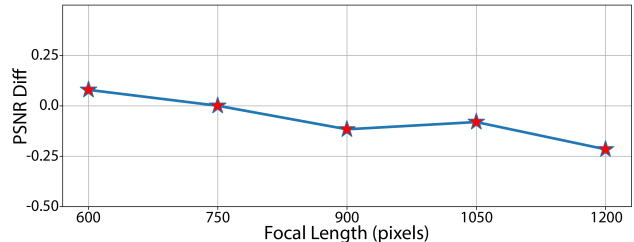


Figure 6. Visual plots showing the performance of GeoFill with different focal lengths. PSNR diff is computed by using GeoFill with new focal length subtract GeoFill with focal length equals to 750.

B. Initial Guess vs Optimized Result

We demonstrate the importance of our optimization module by comparing the performance of GeoFill with initial estimated parameters and optimized parameters. As shown in Table 5, GeoFill with optimized parameters has substantially better performance. Initial parameters are computed from SIFT and pretrained models such as OANet, which can make erroneous predictions, especially for image pairs with holes. Experimental results demonstrate our optimization module successfully mitigates such errors and improves the inpainting performance.

C. Performance w.r.t Intrinsic Parameters

GeoFill handles incoming image pairs using fixed camera intrinsic parameters instead of explicitly knowing the ground-truth camera intrinsic parameters. In the main paper, we use fixed camera intrinsic parameters by setting the focal length of all images to 750 pixels and the principal point to the center of the image. It is intuitive to set the principal point to the center of the images with unknown intrinsic parameters, therefore, we focus on studying the effect of focal lengths. We compare the performance of GeoFill with the camera focal lengths of 600, 750, 900, 1050, and 1200 pixels. As shown in Figure 6, GeoFill with different focal lengths has very slight differences in terms of PSNR. There is a slight trend that the performance drops as the focal length increases. We believe this indicates that the ground-truth focal length is close to 600 and higher focal lengths make the optimization have a harder time finding improved relative poses. Nevertheless, GeoFill can still adapt to different focal lengths by jointly optimizing depth scale, offset, and relative pose, therefore, it still can render similar images across a variety of focal lengths.

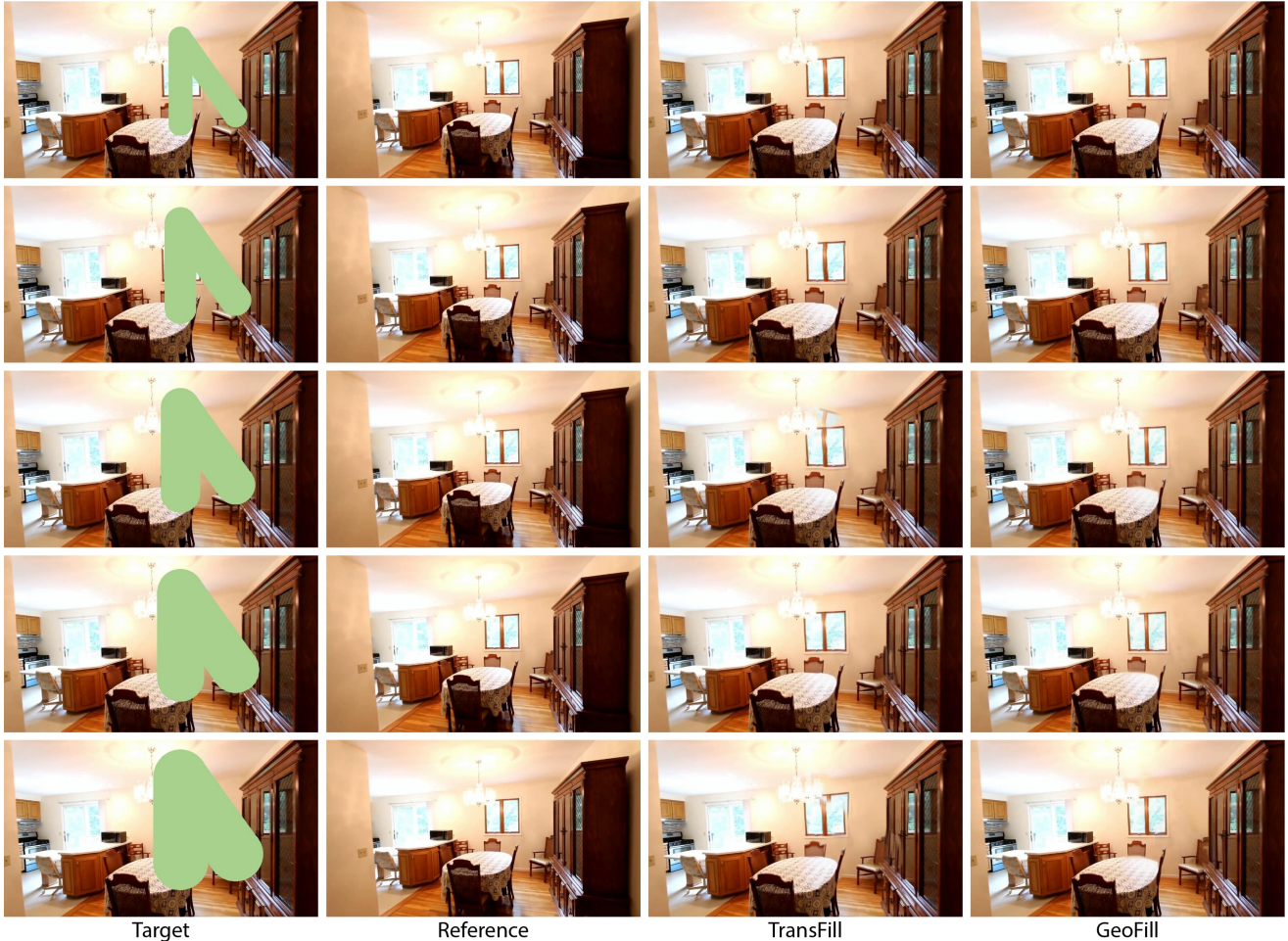


Figure 7. Qualitative comparisons of our approach against TransFill with different hole sizes.

D. Visualizations for Hole Ablation Study

In the main paper, we show the quantitative comparisons between our approach and TransFill with various hole sizes. Here, we provide visual comparisons to better understand the performance boost for larger holes. We simulate larger holes by generating the same hole shape with larger stroke width. As shown in Figure 7, GeoFill has a robust performance while TransFill has ghosting artifacts and misalignments as the hole grows larger.

E. Visualizations of Initial Alignments

GeoFill adopts the CST module from TransFill to further improve any small residual spatial misalignments and correct color and exposure differences. Here, we visually compare the quality of our single proposal to the merged proposal from TransFill without CST. As shown in Figure 8, the single proposal from GeoFill is significantly more accurate than merged heuristic proposals from TransFill, demonstrating the superiority of our approach over TransFill.

Table 6. User study results of GeoFill against ProFill, OPN, and TransFill.

Model	Filtered		Non-Filtered	
	PR	p-value	PR	p-value
ProFill	100%	$p < 10^{-6}$	96.25%	$p < 10^{-6}$
OPN	97.37%	$p < 10^{-6}$	95.00%	$p < 10^{-6}$
TransFill	70.90%	$p < 2 \times 10^{-3}$	68.13%	$p < 2 \times 10^{-3}$

F. User Study

To better evaluate the performance of GeoFill against other baselines, we conduct a user study via Amazon Mechanical Turk (AMT). We compare our method against OPN, ProFill, and TransFill by showing users image pairs with binary choice questions. The users are requested to choose the inpainting results that look more realistic and faithful. To improve the quality of collected data, we adopt a qualification test with trivial questions to filter noisy results. For each method pair, we randomly sampled 80 examples in RealEstate10K dataset with FD=50, and each example was evaluated by 7 independent users. We present

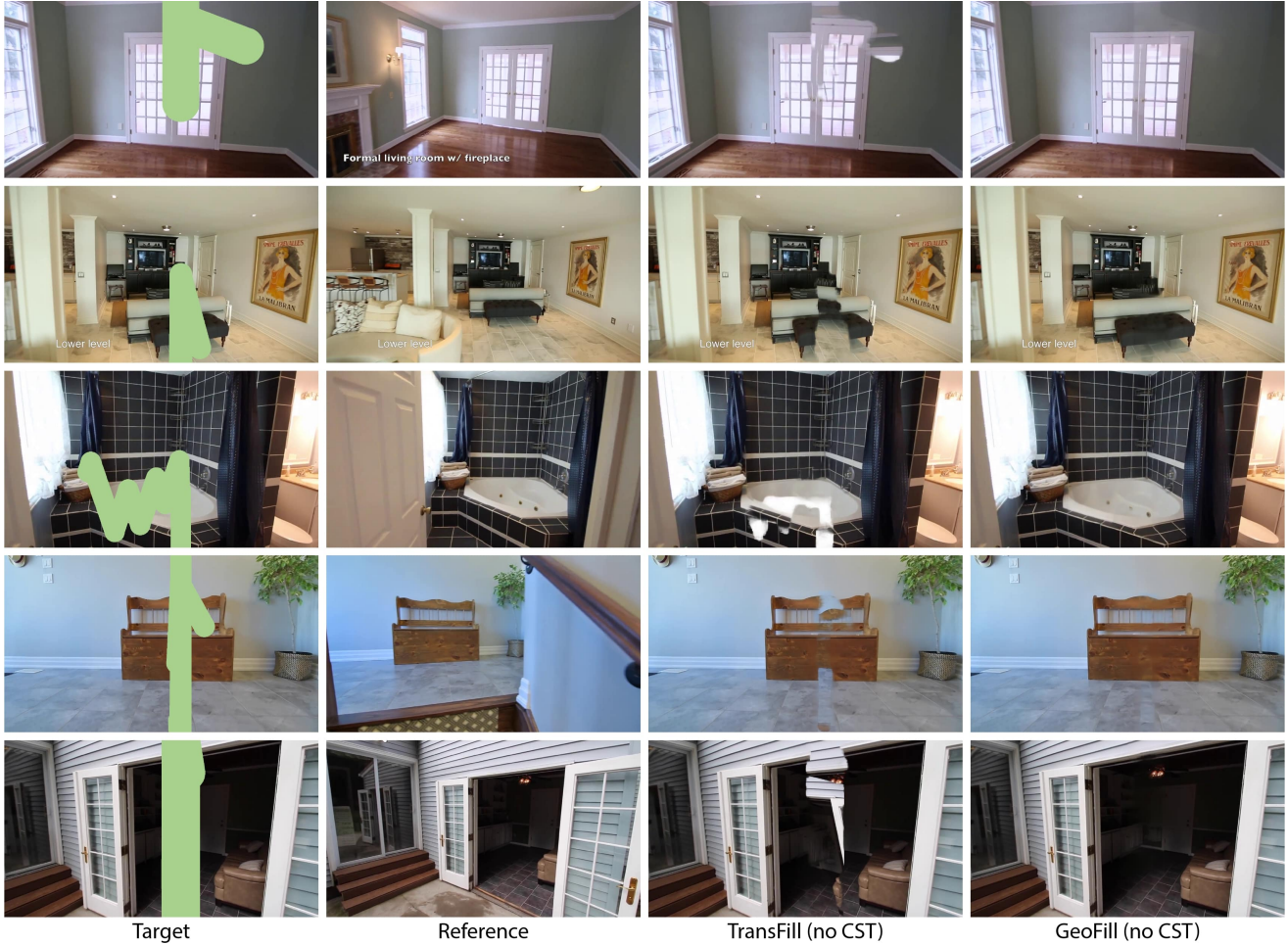


Figure 8. Visual comparisons of GeoFill and TransFill without the CST module.



Figure 9. Visual examples of failure cases of GeoFill.

two approaches to computing the preference rate. The first one is the filtered approach, in which we filter the responses to retain only those where one method is “preferred” if 6 or more users select it. The filtering helps suppress noise in the responses of Mechanical Turk workers, whose work quality can vary. The second one is the non-filtered approach where we retain all responses and choose the method as “preferred” where a simple majority of 4 or more users select it. We reported GeoFill’s Preference Rate (PR) in Table 6. GeoFill has much higher preference rates against

OPN and ProFill. Compared against TransFill, we receive a PR around 70% on filtered and non-filtered approaches. TransFill is still very robust on small holes and relatively small camera motions in the randomly sampled data. Therefore, GeoFill is favored by users over TransFill but less strongly than in the other comparisons. We performed a one sample permutation t test with 10^6 simulations using the null hypothesis that each pair are preferred equally by users: the p-values are all sufficiently small that the preference for our method is statistically significant.

G. Failure Cases

We show some failure cases of GeoFill under extreme conditions. Figure 9 shows three common failure cases of GeoFill. The image pair in the first row contains transparent or specular surfaces in the images. These objects often cause monocular depth estimators to fail and can lead to bad parameters. In the second failure case, GeoFill suffers from the drastically changes in lighting environment. In the last case, dynamic objects, e.g., pedestrians, make our optimization module estimate inaccurate parameters. We discuss in the last section of our main paper ways that future work might address these issues.

Additional Visual Results

We include additional qualitative comparisons of GeoFill against other baselines in Figure 10. Additionally, we also show the inpainting performance of GeoFill on user-provided images, RealEstate10K, and MannequinChallenge dataset in Figure 11.

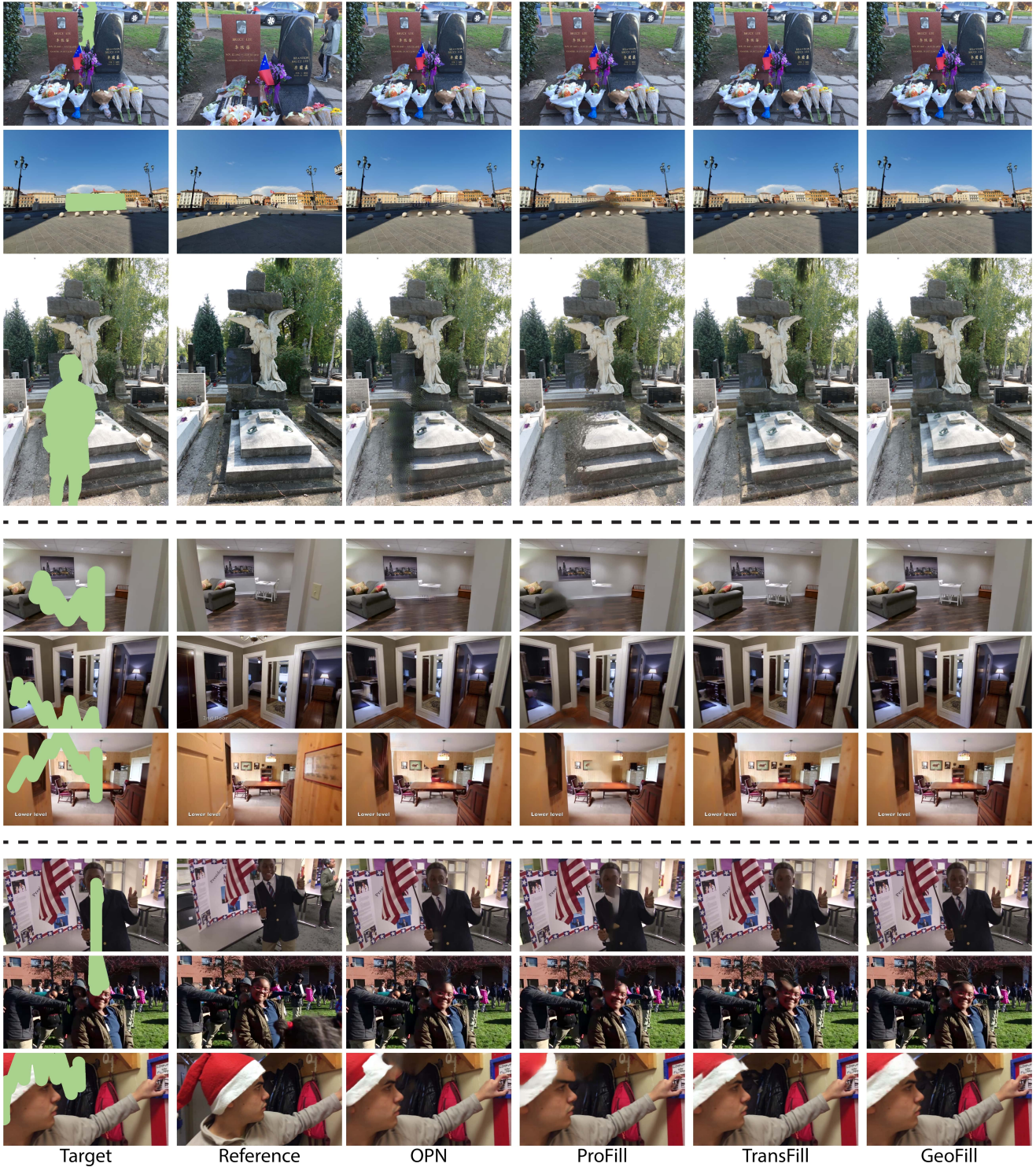
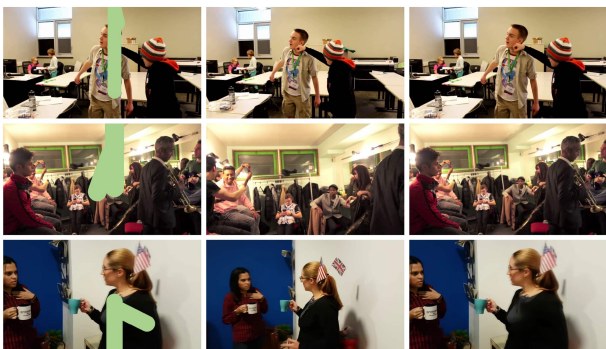
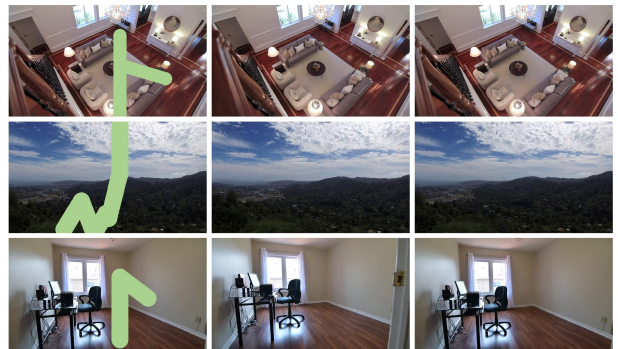
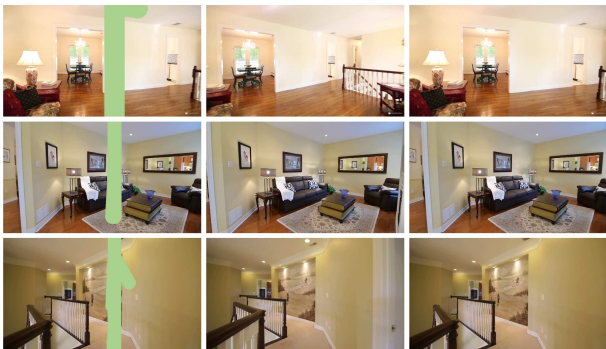
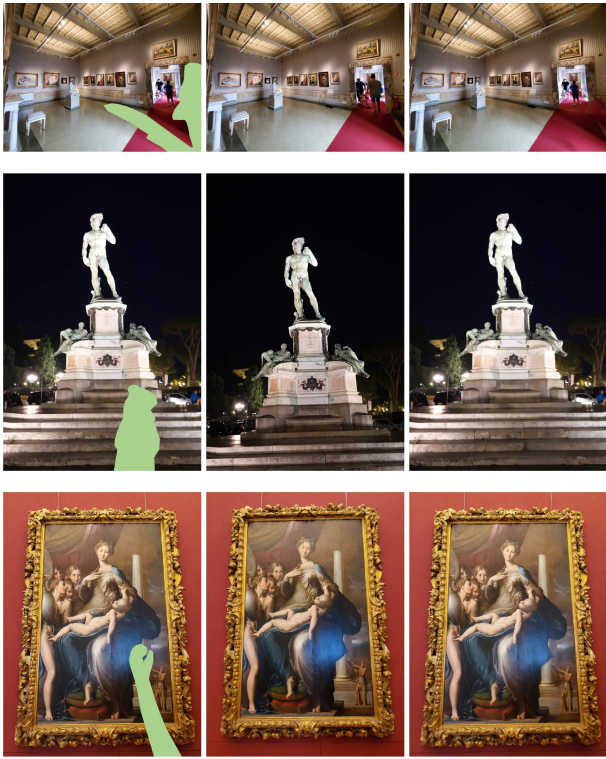


Figure 10. Qualitatively comparison of GeoFill against other baselines on user-provided images (top 3 rows), RealEstate10K (mid 3 rows), and MannequinChallenge dataset (last 3 rows).



Target

Reference

GeoFill

Target

Reference

GeoFill

Figure 11. Visual illustration of inpainting performance of GeoFill on user-provided images, RealEstate10K, and MannequinChallenge dataset.